# 24-hour evolution of an exceptional HONO plume emitted by the record-breaking 2019/2020 Australian Wildfire tracked from space: role of heterogeneous photoinduced production

**G. Dufour[1], M. Eremenko[2], G. Siour[2], P. Sellitto[2], J. Cuesta[2], A. Perrin[3], and M. Beekmann[1]**

[1]Université de Paris and Univ Paris Est Creteil, CNRS, LISA, F-75013, Paris, France.

[2]Univ Paris Est Creteil and Université de Paris, CNRS, LISA, F-94010, Créteil, France.

[3]LMD/IPSL, École Polytechnique, Institut Polytechnique de Paris, ENS, PSL Université, Sorbonne Université, CNRS, Palaiseau, France.

Corresponding author: Gaëlle Dufour (gaelle.dufour@lisa.ipsl.fr)

**Key Points:**

- Tracking HONO fire plumes at free tropospheric levels by IR sounders
- Persistent HONO concentrations observed at sunrise
- Importance of primary fire emissions and heterogeneous photo-induced reaction for modelling the HONO plume

## Abstract

Mega-fires have occurred in Australia during the 2019/2020 bushfire season, leading to enhanced concentrations of many tropospheric pollutants. Here we report on a fire plume with unusually high and persistent HONO levels that we could tracked during one day at free tropospheric levels over the Tasman Sea on 4 January 2020 using IASI and CrIS satellite observations. HONO concentrations up to about 8 ppb were retrieved during nighttime. Persistent HONO concentrations (>1ppb) were still observed at sunrise. Model simulations suggest a significant contribution of primary fire emissions and heterogeneous photo-induced reactions to explain the observed concentrations. However, many uncertainties and unknowns remain in the plume aerosol load and in the chemical processes which may explain the model inability to reproduce HONO concentrations at sunrise.



## Plain Language Summary

Mega-fires have occurred in Australia during the 2019/2020 bushfire season, called the Australian Black Summer. They led to enhanced concentrations of many tropospheric pollutants in the Southern Hemisphere. Amongst them, HONO plays a key role for oxidative capacity of the atmosphere. An exceptional HONO plume with concentrations up to 8 ppb, has been tracked during one day between 5 and 15 km over the Tasman Sea on 4 January 2020 by satellite instruments. If HONO nighttime production is well known, persistence of high HONO concentrations at sunrise one day after the emissions is unusual. Model simulations suggest a significant contribution of primary fire emissions and heterogeneous photo-induced reactions to explain the observed concentrations. However, many unknowns remain in the plume aerosol load and in the chemistry which may explain the model inability to reproduce HONO concentrations at sunrise.


## 1 Introduction

Nitrous acid (HONO) is one of the primary sources of hydroxyl radicals (OH) by photolysis and then plays a key role in tropospheric chemistry for the oxidative capacity of the atmosphere (Finlayson-Pitts & Pitts, 1999). Primary emissions of HONO in the atmosphere are from combustion (e.g. Aumont et al., 2003) and soils (Stemmler et al., 2006). Its secondary production proceeds through the gas phase reaction of NO and OH and by reactions of nitrogen-containing compounds and especially $NO_2$ on surfaces or on aerosols (Aumont et al., 2003; Finlayson-Pitts & Pitts, 1999). Rapid photolysis during daytime is the main HONO sink and leads to a short lifetime in the order of tenths of minutes around local noon, which limits HONO concentrations during daytime. However, large daytime HONO concentrations have already been reported by several studies pointing at unknown or not well quantified sources, such as photo-induced heterogeneous formation (e.g. Kleffmann, 2007; Lu et al., 2018; Neuman et al., 2016). At night, without fast photo-dissociation, HONO tends to accumulate in the atmosphere to light-independent heterogeneous formation on surfaces. The HONO distribution throughout the troposphere is not well known (e.g. J. Kleffmann & Wiesen, 2008) compared to the near surface. Wildfires can have a significant impact on HONO concentrations in the troposphere. Aircraft and ground based measurements have been made but mainly in the planetary boundary layer (PBL) (e.g. Neuman et al., 2016; Peng et al., 2020). Satellite detections have been reported for the IASI instrument in Australian fires in 2009 and 2019 (Clarisse et al., 2011; Longueville et al., 2021) and an estimation of HONO volume mixing ratio (vmr) in the 2009 plume is provided over sea by Armante et al. (2021). Recently, TROPOMI has shown capabilities to cartography the HONO emitted by fires

(Theys et al., 2020). The aforementioned study is restricted to regions close to the sources and does not show any tracking of HONO in dispersed fire plumes over sea. In the present study, we focus on satellite-based detection of HONO during the record-breaking 2019/2020 Australian bushfire season (also called the Australian Black Summer). These mega forest fires burnt an unprecedented area of about 5.8 million hectares, which is more than 20% of whole Australian temperate forests amount (Boer et al., 2020). This historically-relevant fire season was active from September 2019 to March 2020. The concentrations of many tropospheric pollutants were enhanced, in the Southern Hemisphere, since the early phases of the fire season (Kloss et al., 2021). By the way, the intensity of the fires escalated and had a peak in intensity starting from New Year's Eve 2019/2020 to early January 2020, and led to extreme pyro-convective clouds events and the formation of a self-sustained smoke-charged vortex that polluted the stratospheric trace gases and aerosol composition at the Hemispheric spatial scale (Khaykin et al., 2020). We report here on HONO plume detections and transport at relatively high altitude (free troposphere) using successive overpasses of 4 infrared (IR) sounders i.e. CrIS and a series of IASI instruments, during the most intense phase of the 2019/2020 Australian fires in early January 2020. For the first time, HONO has been quantified along the plume transport almost during 24 hours after emission. The CHIMERE chemistry-transport model (CTM) is used to quantify the processes leading to such a plume. In Section 2, we describe the satellite instruments, the detection and retrieval methods as well as the model and simulations experiments performed. In Section 3, a description of the HONO plume crossing the Tasman Sea at free tropospheric levels is given by the observations and the model. The dominant chemical processes leading to such an event is discussed. Conclusions are drawn afterwards.

## 2 Data and Methods

### 2.1 IASI

The IASI (Infrared Atmospheric Sounding Interferometer) instruments are nadir-viewing Fourier transform spectrometers (Clerbaux et al., 2009). Three versions of the instrument are currently flying on board the EUMETSAT (European Organisation for the Exploitation of Meteorological Satellites) Metop satellites on a morning orbit (9:30LST and 21:30LST equator crossing times): one aboard the Metop-A platform since October 2006, one aboard the Metop-B platform since September 2012, and one aboard the Metop-C platform since November 2018. The IASI instruments operate in the thermal infrared between 645 and 2760 $cm^{-1}$ with an apodized resolution of 0.5 $cm^{-1}$ and a radiometric noise of about 0.2K around 1000 $cm^{-1}$. Each IASI instrument scans the atmosphere with a swath width of 2200 km, allowing a global coverage twice a day, with a field of view of 2 × 2 pixels with 12 km footprint at nadir. Metop-A, Metop-B, and Metop-C temporal difference is ~30 min.

### 2.2 CrIS

The CrIS (Cross-track Infrared Sounder) instrument is a Fourier transform spectrometer aboard the Suomi National Polar-orbiting Partnership (S-NPP) platform, in a sun-synchronous low Earth orbit with overpass times of ~01:30 and 13:30 local time. Two CrIS instruments are flying, the first one since October 2011 and the second one since November 2017. In this study, we use the first of these. CrIS scans the atmosphere with a swath width of 2200 km and a field of view of 3 × 3 pixels of 14 km diameter at nadir. CrIS is a hyperspectral infrared instrument with an

unapodized spectral resolution of 0.625 $cm^{-1}$ and low spectral noise of ~0.04K in its long-wave infrared band 1 (648.75-1096.25 $cm^{-1}$) (Han et al., 2013; Strow et al., 2013; Tobin et al., 2013).

### 2.3 HONO spectral ratio and retrieval method

We use the spectral window between 785 and 795 $cm^{-1}$ for HONO detection and retrievals (Fig. S1). For HONO the spectroscopic parameters originate from a preliminary version of the linelist for the $\nu_4$ bands of the HONO Trans- and Cis- conformers that is now available in the GEISA database (Armante et al., 2021; Delahaye et al., 2021). The selected 785-795 $cm^{-1}$ microwindow corresponds to the HONO trans-$\nu_4$ band, where the line intensities are about 12% larger than in Armante et al. (2021). This is largely within the estimated accuracy associated to this entity (about 30%). Carbon dioxide and water vapor are the two main interferers in this window. Their spectroscopic data are taken from HITRAN 2004 (Rothman et al., 2005).

The HONO detection is based on the spectral ratio between one wavenumber belonging in the HONO trans-ν4 absorption band and one without HONO and interferers absorption. As IASI and CrIS spectra have different spectral resolution and the IASI spectra are apodized while CrIS spectra are not, we use different definition of the spectral ratio: it is the ratio between the radiances at 790.5 and 789.0 $cm^{-1}$ for IASI and at 790.0 and 788.75 $cm^{-1}$ for CrIS. For this ratio, a threshold is fixed at 0.985 as a first rapid detection of the scenes and days of interest. Then, to spatially delimit the plumes, we use the distribution of the spectral ratios according to the radiance values (Fig S2). Pixels are considered within the HONO plume when their spectral ratio is smaller than the mean of the distribution minus 3σ for the corresponding radiance. The retrieval is performed for the pixels characterized by a positive detection (i.e., the ones individuated as within the plume). For these pixels, the radiative transfer (RT) is modeled using the KOPRA RT model (Stiller et al., 2000) and the retrieval is performed by its inversion module, KOPRAFIT. The lack of information on the HONO variability and vertical distribution in fire plumes does not permit to derive a meaningful covariance matrix for the retrieval. We then use a smoothing constraint following Steck (2002). We use the discrete first-derivative operator as the constraint operator and fix the strength of the constraint to have one degree of freedom for the solution. A vertically constant a priori profile is used. The $CO_2$ and $H_2O$ absorption lines are simultaneously fitted with HONO. The HONO (vertically constant) retrieved volume mixing ratio provides an estimation of the HONO volume mixing ratio for each in-plume pixel, knowing that the maximum of sensitivity ranges from 5 to 15 km altitude according to the averaging kernels. It is worth noting that, due to the particular conditions in the plume (e.g. smoke contamination), convergence of the retrievals is reached for a fraction of all the available pixels..

### 2.4 CHIMERE

CHIMERE v2020r1 is used over a large Australian domain with a horizontal resolution of 25x25 $km^2$ extending from -56 to 10 °N and 105 to 178 °E. The vertical resolution is 15 levels from the ground to 300 hPa. It is driven by WRF regional model version 3.7.1 (Skamarock et al., 2008). A full description of WRF-CHIMERE is available in Menut et al. (2021). CAMS global anthropogenic v4.1 emissions (Granier et al., 2019) for the year 2019 are used. HONO anthropogenic emissions are considered as 1.5% of NOx emissions from traffic and 0.5% of NOx from other sectors. Fire emissions from CAMS GFAS (Kaiser et al., 2012) are considered. No diurnal cycle is applied. The injection height is calculated by the Sofiev et al. (2012) scheme. 80% of the mass is injected around this height and 20% from the ground to this height. NOx fire

emissions are divided into 90% of NO and 10% of $NO_2$. The HONO gaseous chemistry is represented by MELCHIOR2 chemical mechanism described in Menut et al. (2013). HONO heterogeneous formation from $NO_2$ deposition on wet surface is considered, using the Aumont et al. (2003) formulation. The different reactions (R1-R5) are listed in Table 1. This constitutes the reference simulation of the study, named simulation GFAS (Table 1). However, the observed HONO/$NO_2$ ratio close to fire sources suggests that HONO primary emissions can be very high (Theys et al., 2020). In a second simulation, named HONOMAX, we added HONO wildfire emissions as 61% of NOx emissions from GFAS. This corresponds to the upper range of HONO/$NO_2$ enhancement rations observed by Theys et al. (2020). In addition, many studies have suggested an additional source of HONO would be present in the daytime as said before (e.g. Wong et al., 2013). To account for this formation pathway, we added a photolytic HONO formation on aerosol (R6) in a third simulation, named HONOMAXJ (Table 1). The effect of the photolysis is considered as zenithal angle function. For urban Chinese conditions, at local noon, Lu et al. (2018) derived for the collision (reactive uptake) coefficient a range of values from 1 to 8 $10^{-4}$. We retained here a collision coefficient of $10^{-3}$ ($\gamma$ in Table 1), for local noon, which is slightly above the upper range of these estimations and also an order of magnitude larger than the value chosen in Liu et al. (2021) for model simulations in Beijing. All three simulations include the light independent heterogeneous HONO formation pathway. Finally, to quantify the importance of each process, we have added some reactive tracers. Each tracer has the same sinks (chemistry and deposition) as real HONO species. Only the source of each tracer is different: HONO_FIRE for primary fire emissions, HONO_ANT for CAMS anthropogenic emissions, HONO_CHEM for (R1), HONO_SURF for (R4), HONO_AER for (R5), and HONO_AERJ for (R6).

**Table 1**. List of reactions involving HONO included in the CHIMERE simulations and description of the CHIMERE simulations.

| | | | |
|---|---|---|---|
| R1 | NO+OH+M→HONO | $k = \frac{k_0[M]}{1+\frac{k_0[M]}{k_\infty}} f^p$<br>$p = \frac{1}{1+\left(log_{10}\left(\frac{k_0[M]}{k_\infty}\right)\right)^2}$<br>$k_0 = A_0 e^{\left(-\frac{B_0}{T}\right)}\left(\frac{T}{300}\right)^{-n_0}$<br>$k_\infty = A_\infty e^{\left(-\frac{B_\infty}{T}\right)}\left(\frac{T}{300}\right)^{-n_\infty}$<br>$A_0$=7x10$^{-31}$, $B_0$=0, $n_0$=2.6<br>$A_\infty$=1.5x10$^{-11}$, $B_\infty$=0, $n_\infty$=0.5<br>f=0.6 | Atkinson et al. (1997) |
| R2 | HONO+OH→NO2 | k(T)=A$e^{-B/T}$<br>A=1.8 ×10$^{-11}$, B =390 | Atkinson et al. (1997) |
| R3 | HONO+hν→NO+OH | $J_{HONO}$ | Burkholder et al. (2010) |
| R4 | NO2→HONO | ks=0.5*depo(NO2) | Aumont et al., 2003 |

| | | | |
|---|---|---|---|
| R5 | NO2→0.5*HONO+0.5*HNO3 | $k_{NO2} = \frac{1}{4}\gamma\langle c\rangle S_a$ <br> $\gamma$=5x10$^{-5}$ | Tang et al., (2014) |
| R6 | NO2+hν→HONO | $k_{NO2} = \frac{1}{4}\gamma\langle c\rangle S_a max(cos(\theta_S),0)$ <br> $\gamma$=1×10$^{-3}$ | Wong et al., (2013) |
| Simulation GFAS | | R1-R5 and GFAS emissions | |
| Simulation HONOMAX | | Simulation GFAS + HONO primary emissions as 61% of NOx | |
| Simuation HONOMAXJ | | Simulation HONOMAX + R6 | |

## 3 Results and discussion

### 3.1 HONO plume detection and tracking from satellite observations

The rapid preliminary screening detection procedure based on the spectral ratio has been first applied to the entire IASI-A archive since 2007. Two main HONO detections have been found during the 2009 Australian fires already reported in literature (Armante et al., 2021; Clarisse et al., 2011) and during the record-breaking Australian fires, which occurred from the end of 2019 to early 2020. For the latter where an intense and well-shaped plume has been detected on 4 January 2020 and is subsequently analyzed in detail. Using combined IASI-A, IASI-B, IASI-C, and CrIS data, we are able for the first time to follow a HONO fire plume over a full day with several overpasses, which enables us to follow the temporal evolution of its concentrations. We are then able to track the plume from Southeast Australia (South of Canberra) on 4 January 2020 04:00 UTC to West of the northern edge of New-Zealand on 5 January 2020 02:00 UTC across the Tasman Sea. We consider the detected plume only where it is fully sampled by the satellite instruments (in the middle of the swath and not in the border). Figure 1 shows the plume trajectory and displays the HONO vmr observed during the plume transport. The plume forward trajectory is calculated with the HYSPLIT model (Rolph et al., 2017; Stein et al., 2015) initialized at the mean location (latitude, longitude) of the plume detected by CrIS at 04:00 UTC and constrained by the Global Data Assimilation System (GDAS). As the satellite observations are broadly sensitive from 5 to 15 km, we tested different initialization heights and searched for the ones matching the center of the plume detected with IASI and CrIS for the following 24 hours. Both 7 km and 9 km initializations succeed to reproduce the satellite-based trajectory. When initialized at 7 km the air mass remains within 6 and 7 km during the plume transport to New-Zealand a day after. At 9 km, the air mass is rapidly uplifted between 11 and 12 km and then moved on at constant altitude (Fig. S3). The height of the plume in the free or upper troposphere is consistent with the detection capabilities of the IR sounders, which are mostly sensitive to this atmospheric region due to large temperature differences with respect to the surface. It is also worth noting that in January 2020 extreme pyro-convection kicked-off, linked to this fire event, leading to the injection of fire-related gaseous and particulate emissions in the stratosphere, at altitudes larger than 17 km (Khaykin et al., 2020). The smoke-charged vortex plume was lifted, in the following two months, by in-plume radiative heating to altitudes as high as 35 km. The initial uplifting tendency of the plume is also visible in our present trajectories analyses. Unfortunately, CALIOP measurements are not available for that day to help identifying the plume height.

Figure 1 shows the evolution of the HONO vmr during the transport of the plume from Southeast Australia to New-Zealand. HONO vmr increases between 4UTC and 11UTC when night starts. Then, a slow decrease is observed from sunrise onwards when HONO is photolyzed but with observed vmr still higher than 1 ppb. As the retrievals may fail when aerosol load is strong, typically at the center of the plume, and lead to an underestimation of mean HONO concentrations we also consider in the following the 90-percentile, which is more representative of the central region of the plume where dilution with background air is reduced and the aerosol light extinction is larger reducing HONO photolysis (during daytime) (Peng et al., 2020). The retrieved concentrations range between 1.3 to 2.9 ppb on average, 2.1 to 5.5 ppb in the center of the plume (90-percentile) (Fig. 3, red symbols). It is worth noting these vmrs are consistent with the HONO vmrs estimated in the 2009 plume by Armante et al. (2021). In 2020, the concentrations increase during the night and reach 2.9 ppb on average, 5.5 ppb in the center of the plume at 11:30UTC and then start to decrease progressively when sun rises and drop to 1.3 ppb on average (2.1 in the center of the plume) at 2UTC on 5 January 2020. This range of concentrations are consistent with HONO concentrations measured in fire plumes, mainly in the U.S, during field and airborne campaigns (e.g. Neuman et al., 2016; Zarzana et al., 2017, Kaspari et al., 2021). However, compared to HONO concentrations reported in the literature, the HONO concentrations retrieved from CrIS and IASI likely correspond to plumes much higher in altitude than the ones sampled during airborne campaigns, so that they are not clearly comparable. The fuel power of the 2019/2020 Australian fire was likely strong enough to emit large quantities of NOx and HONO and to uplift the emitted fire products higher than usual in the atmosphere, allowing a better detection from IR sounders. Satellite observations show production of HONO within the plume during the night, as HONO concentrations increase albeit plume diffusion. Then, significant HONO concentrations (about the half of the maximal nighttime values) surprisingly remain in the plume even after sunrise, suggesting that HONO photolysis may be counterbalanced by production within the plume. Such a mechanism has been recently reported by Kaspari et al. (2021) but for measurements near the surface where the heterogeneous secondary production of HONO is increased by the ground surface.

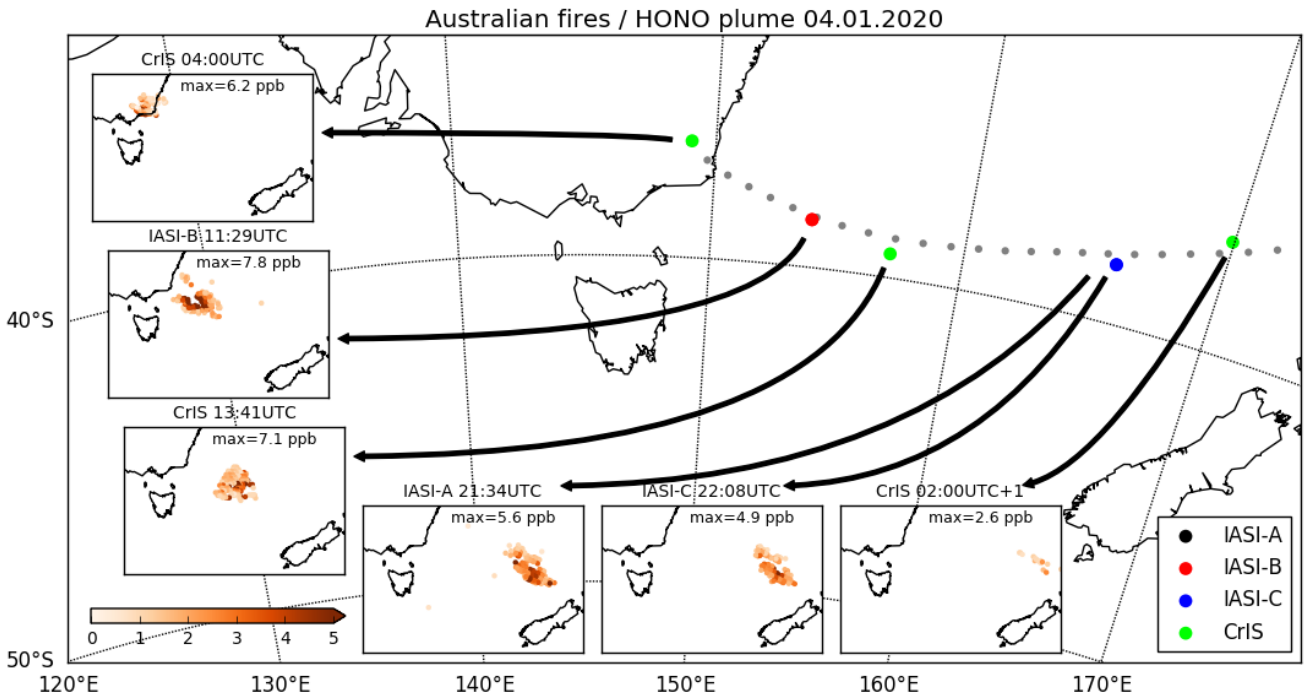


Figure 1. HONO plume tracking by CrIS and IASI instrument. HYSPLIT trajectory (initialized at 7 km – similar when initialized at 9 km). Normalized spectral ratios.

### 3.2 Simulated HONO plume with CHIMERE

We use the CTM CHIMERE to simulate HONO in the 2019/2020 Australian fires as described in section 2.4. Simulating correct HONO concentrations is a great challenge for models due to the large uncertainties in the fire emissions (location, intensity, emission factors, injection height etc), their HONO fraction, and plume chemistry, in particular heterogeneous HONO formation, photo-induced or not. CHIMERE simulations are then mainly used to evaluate different HONO temporal evolutions within the fire plume rather than absolute concentrations. For 4 January 2021, the model simulates a HONO plume similar to the one detected by the satellite instruments. The simulated plume starts in the vicinity of Canberra, northward compared to the observed plume (Fig. 2). The plume extends up to the level 12 of the model between 6 and 7 km. The upper part of the plume (level 11 around 5 km and level 12 between 6-7km) moves faster and further away above the Tasman Sea towards the western part of New Zealand. Due to the vertical sensitivity of IR sounders and the forward trajectories coherent with the detected plumes, we focus on these two levels for the analysis of the three simulations detailed in Section 2.4.

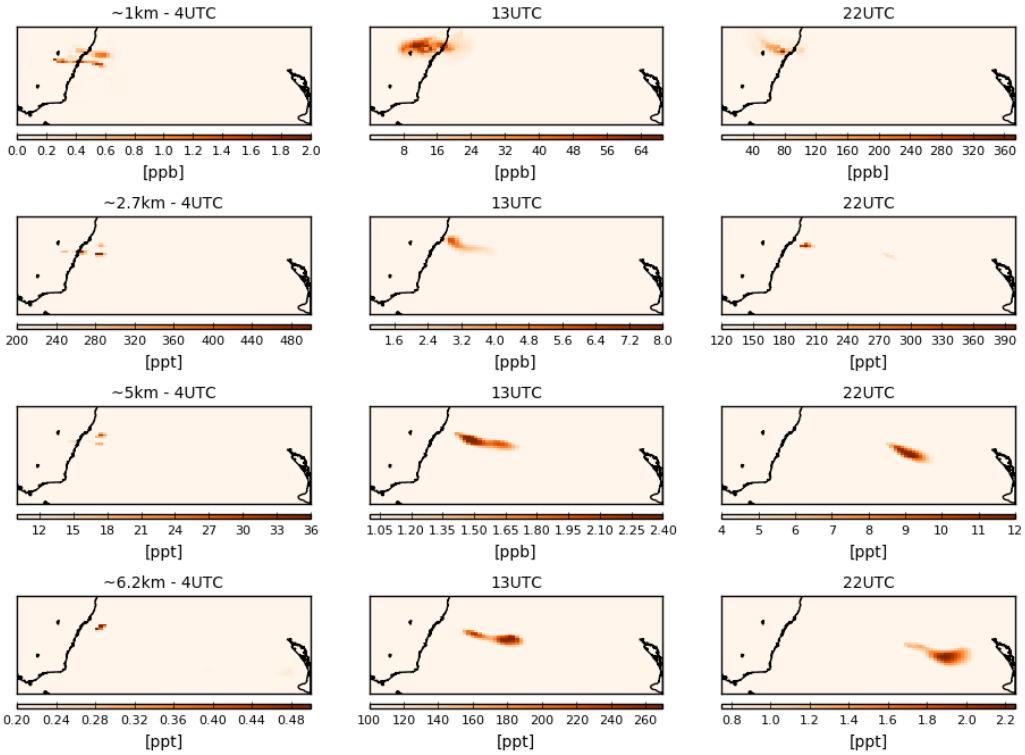


Figure 2. Simulated HONO concentrations within the plume (simulation GFAS) at different levels (levels 5 (~1km), 9 (~2.7km), 11 (~5km), and 12 (~6.2km)) and hours of 4 January 2020.

At the maximum, the HONO vmr simulated by the GFAS simulation reaches about 0.2 ppb in the plume at level 12 and 1.3 ppb on average (2 ppb for 90-percentile) at level 11 (Fig. 3). Compared to satellite observation, these concentrations are largely underestimated at level 12 (~6.2km), which is closer to the altitude range of the satellite sensitivity. When including the primary HONO emissions (HONOMAX), the HONO vmr increases to about 0.4 ppb on average in the plume (0.6 ppb 90-percentile) at level 12 and to about 3 ppb on average (5 ppb 90-percentile) at level 11. Including the heterogeneous photo-induced reaction of $NO_2$ increases HONO levels closer to 1 ppb (1.4 ppb 90-percentile) at level 12 and then closer to the order of magnitude of HONO observed by IR sounders. At level 11, HONO reaches at maximum 5 ppb (11 ppb 90-percentile) when this reaction is considered. However, because of the uncertainty in injection height, it is not possible to favor one of the three simulations from this first comparison. In terms of process contributions, the photo-induced heterogeneous reaction dominates the HONO production in the plume when included, followed by HONO_AER (light independent heterogeneous reaction) and the contribution from primary emissions (Fig. S4). Analyzing the temporal evolution shows interesting differences between the three simulations (Fig. 3). They all show a rapid increase of HONO at the night between 9 and 11 UTC. The increase is more progressive at level 11 especially for the HONOMAXJ simulation because HONO is formed more strongly at the end of the first

day due to the photo-induced heterogeneous reaction. An abrupt decrease is observed for all the simulations between 19 and 20 UTC, at the beginning of the next day. While HONO concentrations without a photo-induced HONO source rapidly drop to near zero at day time, the one including such a source shows significant HONO levels for the early morning hours, about 0.5 (average) to 0.8 ppb (P90) at level 11 at 21 UTC. However later on, they also show HONO concentrations close to zero (few ppt or less). The amplitude of this drop-off is much stronger than the one observed with the data, even for the simulation including the photo-induced reaction. This could either suggest a model overestimation of HONO sinks (i), or of HONO plume dilution (ii), or an underestimation of HONO sources. Concerning HONO photodissociation the aerosol induced actinic flux attenuation is included in the model, but the photodissociation rate may be biased high, if aerosol mass is biased low. Dilution of the plume certainly plays a role in reducing HONO levels, but this process is expected to happen continuously and not only at sunrise. Finally, our study suggests the possibility the photoinduced collision coefficient (R6) of $10^{-3}$ (at cloud free local noon), at the upper end of values given in available literature ($10^{-4}$ - $10^{-3}$ as discussed in section 2.4), might still be underestimated. Alternatively or in addition, available aerosol surface might be higher than estimated by our model assuming spherical particles. For example, fire aerosol can be highly porous through the formation of soot aggregates (Chakrabarty et al., 2014). These hypotheses warrant for further studies.

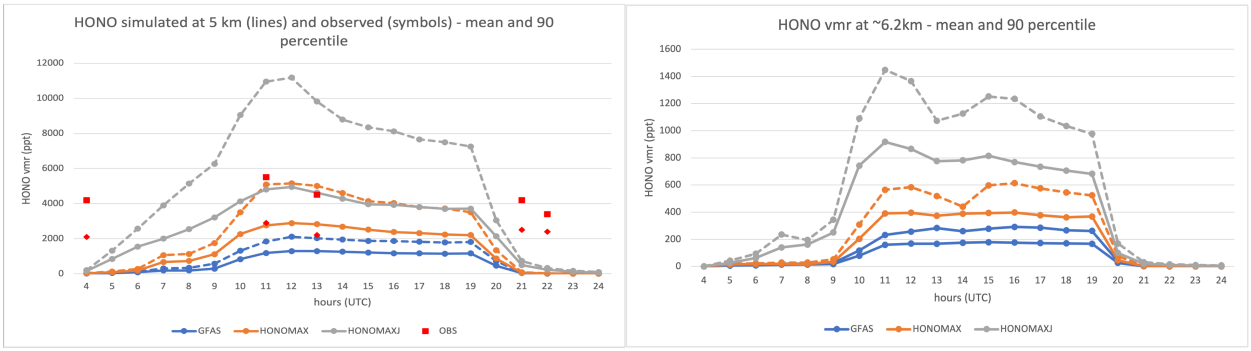


Figure 3. Temporal evolution of HONO simulated at 11km and 12km by CHIMERE for the three simulation experiments described in Table 1. Mean vmr are represented as full lines and 90-percentile vmr as dashed lines.

## Conclusions

For the first time, a HONO plume emitted by the record-breaking 2019/2020 Australian fires has been tracked, and its evolution quantified, during one day above the Tasman Sea by four IR sounders, the three IASI and CrIS. HONO vmrs of several ppb have been retrieved within the plume. The remarkable points rise from the transport at free tropospheric altitudes (or higher) of the plumes (or higher) and the persistence of large HONO vmr (>1ppb) after one day during sunrise. Model simulations, aiming at reproducing this exceptional event, confirm that the plume is transported in the free troposphere and suggest a significant contribution of primary fire emissions of HONO and of photo-induced heterogeneous reactions to explain the observed HONO vmrs. However, despite this, the question of the processes involved to explain the persistent HONO concentrations at sunrise is not fully resolved, the model showing a much stronger decrease of

HONO when the sun rises, which points to remaining unknowns in chemistry and aerosol loading in the plume.

## Acknowledgments

The authors acknowledge the different data centers to make satellite and emission data available: the Data and Service for the Atmosphere (AERIS) portal and the NASA GESDISC system. The authors gratefully acknowledge the NOAA Air Resources Laboratory (ARL) for the provision of the HYSPLIT model and/or READY website used in this publication. We acknowledge the Institut für Meteorologie und Klimaforschung (IMK), Karlsruhe, Germany, for a licence to use the KOPRA radiative transfer model. This work was granted access to the HPC resources of TGCC under the allocation 7232 made by GENCI (Grand Equipement National de Calcul Intensif).
The IASI mission is a joint mission of EUMETSAT and the Centre National d'Etudes Spatiales (CNES, France). This study was financially supported by the French Space Agency – CNES (project "IASI/TOSCA" and "IASI-NG/TOSCA").

## Open Research

The IASI Level 1C data used for the HONO observations in fire plumes in the study are available at the French Data and Service for the Atmosphere (AERIS) portal via https://iasi.aeris-data.fr/ with registration.
The CrIS Level 1 data used for the HONO observations in fire plumes in the study are available at the GES DISC NASA portal via https://sounder.gesdisc.eosdis.nasa.gov/data/SNPP_Sounder_Level1/SNPPCrISL1BNSR.2/ with registration.
V2020r1 of the CHIMERE model used for simulating HONO in Australian fire plumes is preserved at https://www.lmd.polytechnique.fr/chimere/, available via the GNU General Public License with registration and developed openly at https://www.lmd.polytechnique.fr/chimere/.
The emission inventory data used for the HONO simulations as input of the CHIMERE model are available at the French Data and Service for the Atmosphere (AERIS) portal via https://eccad.aeris-data.fr/ with registration.
Version 5.1.0 of the HYSPLIT transport and dispersion model used to calculate trajectories of fire plumes in this study is preserved at https://www.ready.noaa.gov, available openly through the website and developed openly at https://www.ready.noaa.gov.

## References

Armante, R., Perrin, A., Kwabia Tchana, F., & Manceron, L. (2021). The ν4 bands at 11 μm: linelists for the Trans- and Cis- conformer forms of nitrous acid (HONO) in the 2019 version of the GEISA database*. *Molecular Physics*, *0*(0), e1951860. https://doi.org/10.1080/00268976.2021.1951860

Aumont, B., Chervier, F., & Laval, S. (2003). Contribution of HONO sources to the NOx/HOx/O3 chemistry in the polluted boundary layer. *Atmospheric Environment*, *37*(4), 487–498. https://doi.org/10.1016/S1352-2310(02)00920-2

Boer, M. M., Resco de Dios, V., & Bradstock, R. A. (2020). Unprecedented burn area of Australian

348 mega forest fires. *Nature Climate Change*, *10*(3), 171–172. https://doi.org/10.1038/s41558-020-
349 0716-1
350 Chakrabarty, R. K., Beres, N. D., Moosmüller, H., China, S., Mazzoleni, C., Dubey, M. K., et al.
351 (2014). Soot superaggregates from flaming wildfires and their direct radiative forcing. *Scientific*
352 *Reports*, *4*(1), 5508. https://doi.org/10.1038/srep05508
353 Clarisse, L., R'Honi, Y., Coheur, P. F., Hurtmans, D., & Clerbaux, C. (2011). Thermal infrared
354 nadir observations of 24 atmospheric gases. *Geophysical Research Letters*, *38*(10).
355 https://doi.org/10.1029/2011GL047271
356 Clerbaux, C., Boynard, A., Clarisse, L., George, M., Hadji-Lazaro, J., Herbin, H., et al. (2009).
357 Monitoring of atmospheric composition using the thermal infrared IASI/MetOp sounder.
358 *Atmospheric Chemistry and Physics*, *9*(16), 6041–6054. https://doi.org/10.5194/acp-9-6041-2009
359 Delahaye, T., Armante, R., Scott, N. A., Jacquinet-Husson, N., Chédin, A., Crépeau, L., et al.
360 (2021). The 2020 edition of the GEISA spectroscopic database. *Journal of Molecular*
361 *Spectroscopy*, *380*, 111510. https://doi.org/10.1016/j.jms.2021.111510
362 Finlayson-Pitts, B., & Pitts, J. Jr. (1999). *Chemistry of the Upper and Lower Atmosphere - 1st*
363 *Edition* (Academic Press). Retrieved from https://www.elsevier.com/books/chemistry-of-the-
364 upper-and-lower-atmosphere/finlayson-pitts/978-0-12-257060-5
365 Granier, C., Darras, S., Denier van der Gon, H., Doubalova, J., Elguindi, N., Galle, B., et al. (n.d.).
366 The Copernicus Atmosphere Monitoring Service global and regional emissions (April 2019
367 version). https://doi.org/10.24380/D0BN-KX16
368 Han, Y., Revercomb, H., Cromp, M., Gu, D., Johnson, D., Mooney, D., et al. (2013). Suomi NPP
369 CrIS measurements, sensor data record algorithm, calibration and validation activities, and record
370 data quality. *Journal of Geophysical Research: Atmospheres*, *118*(22), 12,734-12,748.
371 https://doi.org/10.1002/2013JD020344
372 Kaiser, J. W., Heil, A., Andreae, M. O., Benedetti, A., Chubarova, N., Jones, L., et al. (2012).
373 Biomass burning emissions estimated with a global fire assimilation system based on observed
374 fire radiative power. *Biogeosciences*, *9*(1), 527–554. https://doi.org/10.5194/bg-9-527-2012
375 Kaspari, J. H., Chai, J., Anderson, B. E., Jordan, C., Scheuer, E., Hastings, M. G., & Dibb, J. E.
376 (2021, February 4). Influence of Solar Irradiation on Nitrous Acid Production in Western U.S.
377 Wildfire Smoke [preprint]. https://doi.org/10.1002/essoar.10506007.1
378 Khaykin, S., Legras, B., Bucci, S., Sellitto, P., Isaksen, L., Tencé, F., et al. (2020). The 2019/20
379 Australian wildfires generated a persistent smoke-charged vortex rising up to 35 km altitude.
380 *Communications Earth & Environment*, *1*(1), 1–12. https://doi.org/10.1038/s43247-020-00022-5
381 Kleffmann, J., & Wiesen, P. (2008). Technical Note: Quantification of interferences of wet
382 chemical HONO LOPAP measurements under simulated polar conditions. *Atmospheric Chemistry*
383 *and Physics*, *8*(22), 6813–6822. https://doi.org/10.5194/acp-8-6813-2008
384 Kleffmann, Jörg. (2007). Daytime Sources of Nitrous Acid (HONO) in the Atmospheric Boundary
385 Layer. *ChemPhysChem*, *8*(8), 1137–1144. https://doi.org/10.1002/cphc.200700016
386 Kloss, C., Sellitto, P., von Hobe, M., Berthet, G., Smale, D., Krysztofiak, G., et al. (2021).
387 Australian Fires 2019–2020: Tropospheric and Stratospheric Pollution Throughout the Whole Fire
388 Season. *Frontiers in Environmental Science*, *9*, 220. https://doi.org/10.3389/fenvs.2021.652024
389 Liu, J., Liu, Z., Ma, Z., Yang, S., Yao, D., Zhao, S., et al. (2021). Detailed budget analysis of
390 HONO in Beijing, China: Implication on atmosphere oxidation capacity in polluted megacity.
391 *Atmospheric Environment*, *244*, 117957. https://doi.org/10.1016/j.atmosenv.2020.117957
392 Longueville, H. D., Clarisse, L., Whitburn, S., Franco, B., Bauduin, S., Clerbaux, C., et al. (2021).
393 Identification of Short and Long-Lived Atmospheric Trace Gases From IASI Space Observations.

*Geophysical Research Letters*, *48*(5), e2020GL091742. https://doi.org/10.1029/2020GL091742
Lu, X., Wang, Y., Li, J., Shen, L., & Fung, J. C. H. (2018). Evidence of heterogeneous HONO formation from aerosols and the regional photochemical impact of this HONO source. *Environmental Research Letters*, *13*(11), 114002. https://doi.org/10.1088/1748-9326/aae492
Menut, L., Bessagnet, B., Khvorostyanov, D., Beekmann, M., Blond, N., Colette, A., et al. (2013). CHIMERE 2013: a model for regional atmospheric composition modelling. *Geoscientific Model Development*, *6*(4), 981–1028. https://doi.org/10.5194/gmd-6-981-2013
Menut, Laurent, Bessagnet, B., Briant, R., Cholakian, A., Couvidat, F., Mailler, S., et al. (2021). The CHIMERE v2020r1 online chemistry-transport model. *Geoscientific Model Development Discussions*, 1–50. https://doi.org/10.5194/gmd-2021-96
Neuman, J. A., Trainer, M., Brown, S. S., Min, K.-E., Nowak, J. B., Parrish, D. D., et al. (2016). HONO emission and production determined from airborne measurements over the Southeast U.S. *Journal of Geophysical Research: Atmospheres*, *121*(15), 9237–9250. https://doi.org/10.1002/2016JD025197
Peng, Q., Palm, B. B., Melander, K. E., Lee, B. H., Hall, S. R., Ullmann, K., et al. (2020). HONO Emissions from Western U.S. Wildfires Provide Dominant Radical Source in Fresh Wildfire Smoke. *Environmental Science & Technology*, *54*(10), 5954–5963. https://doi.org/10.1021/acs.est.0c00126
Rolph, G., Stein, A., & Stunder, B. (2017). Real-time Environmental Applications and Display sYstem: READY. *Environmental Modelling & Software*, *95*, 210–228. https://doi.org/10.1016/j.envsoft.2017.06.025
Rothman, L. S., Jacquemart, D., Barbe, A., Benner, D. C., Birk, M., Brown, L. R., et al. (2005). The HITRAN 2004 molecular spectroscopic database. *J. Quant. Spectrosc. Radiat. Transfer*, *96*, 139–204. https://doi.org/10.1016/j.jqsrt.2004.10.008
Skamarock, W., Klemp, J., Dudhia, J., Gill, D., Barker, D., Wang, W., et al. (2008). *A Description of the Advanced Research WRF Version 3* [Application/pdf] (p. 1002 KB). UCAR/NCAR. https://doi.org/10.5065/D68S4MVH
Sofiev, M., Ermakova, T., & Vankevich, R. (2012). Evaluation of the smoke-injection height from wild-land fires using remote-sensing data. *Atmospheric Chemistry and Physics*, *12*(4), 1995–2006. https://doi.org/10.5194/acp-12-1995-2012
Steck, T. (2002). Methods for determining regularization for atmospheric retrieval problems. *Applied Optics*, *41*(9), 1788–1797. https://doi.org/10.1364/AO.41.001788
Stein, A. F., Draxler, R. R., Rolph, G. D., Stunder, B. J. B., Cohen, M. D., & Ngan, F. (2015). NOAA's HYSPLIT Atmospheric Transport and Dispersion Modeling System. *Bulletin of the American Meteorological Society*, *96*(12), 2059–2077. https://doi.org/10.1175/BAMS-D-14-00110.1
Stemmler, K., Ammann, M., Donders, C., Kleffmann, J., & George, C. (2006). Photosensitized reduction of nitrogen dioxide on humic acid as a source of nitrous acid. *Nature*, *440*(7081), 195–198. https://doi.org/10.1038/nature04603
Stiller, G. P., von Clarmann, T., Dudhia, A., Echle, G., Funke, B., Glatthor, N., et al. (2000). *The Karlsruhe Optimized and Precise Radiative Transfer Algorithm (KOPRA), vol. FZKA 6487 of Wissenschaftliche Berichte*. (G. P. Stiller, Ed.). Forschungszentrum Karlsruhe, Germany.
Strow, L. L., Motteler, H., Tobin, D., Revercomb, H., Hannon, S., Buijs, H., et al. (2013). Spectral calibration and validation of the Cross-track Infrared Sounder on the Suomi NPP satellite. *Journal of Geophysical Research: Atmospheres*, *118*(22), 12,486-12,496. https://doi.org/10.1002/2013JD020480

Theys, N., Volkamer, R., Müller, J.-F., Zarzana, K. J., Kille, N., Clarisse, L., et al. (2020). Global nitrous acid emissions and levels of regional oxidants enhanced by wildfires. *Nature Geoscience*, *13*(10), 681–686. https://doi.org/10.1038/s41561-020-0637-7

Tobin, D., Revercomb, H., Knuteson, R., Taylor, J., Best, F., Borg, L., et al. (2013). Suomi-NPP CrIS radiometric calibration uncertainty. *Journal of Geophysical Research: Atmospheres*, *118*(18), 10,589-10,600. https://doi.org/10.1002/jgrd.50809

Wong, K. W., Tsai, C., Lefer, B., Grossberg, N., & Stutz, J. (2013). Modeling of daytime HONO vertical gradients during SHARP 2009. *Atmospheric Chemistry and Physics*, *13*(7), 3587–3601. https://doi.org/10.5194/acp-13-3587-2013

Zarzana, K. J., Min, K.-E., Washenfelder, R. A., Kaiser, J., Krawiec-Thayer, M., Peischl, J., et al. (2017). Emissions of Glyoxal and Other Carbonyl Compounds from Agricultural Biomass Burning Plumes Sampled by Aircraft. *Environmental Science & Technology*, *51*(20), 11761–11770. https://doi.org/10.1021/acs.est.7b03517